

Calibration Transfer Methodology for Cloud Radars Based on Ice Cloud Observations

SUSANA JORQUERA^a, FELIPE TOLEDO BITTNER^b, JULIEN DELANOË^a, ALEXIS BERNE^c, ANNE-CLAIRE BILLAULT-ROUX^c, ALFONS SCHWARZENBOECK^d, FABIEN DEZITTER^e, NICOLAS VILTARD^a, AND AUDREY MARTINI^a

^a *Laboratoire Atmosphères, Milieux, Observations Spatiales/UVSQ/CNRS/UPMC, Guyancourt, France*

^b *Laboratoire de Météorologie Dynamique, Institut Pierre Simon Laplace, Ecole polytechnique-IP Paris, ENS-PSL Université, Sorbonne Université, CNRS, Palaiseau, France*

^c *Environmental Remote Sensing Laboratory, École Polytechnique Fédérale de Lausanne, Lausanne, Switzerland*

^d *Laboratoire de Météorologie Physique, Aubière, France*

^e *Airbus Helicopters, Marignane, France*

(Manuscript received 1 August 2022, in final form 7 April 2023, accepted 7 April 2023)

ABSTRACT: This article presents a calibration transfer methodology that can be used between radars of the same or different frequency bands. This method enables the absolute calibration of a cloud radar by transferring it from another collocated instrument with known calibration, by simultaneously measuring vertical ice cloud reflectivity profiles. The advantage is that the added uncertainty in the newly calibrated instrument can converge to the magnitude of the reference instrument calibration. This is achieved by carefully selecting comparable data, including the identification of the reflectivity range that avoids the disparities introduced by differences in sensitivity or scattering regime. The result is a correction coefficient used to compensate measurement bias in the uncalibrated instrument. Calibration transfer uncertainty can be reduced by increasing the number of sampling periods. The methodology was applied between collocated W-band radars deployed during the ICE-GENESIS campaign (Switzerland 2020/21). A difference of 2.2 dB was found in their reflectivity measurements, with an uncertainty of 0.7 dB. The calibration transfer was also applied to radars of different frequency, an X-band radar with unknown calibration and a W-band radar with manufacturer calibration; the difference found was -16.7 dB with an uncertainty of 1.2 dB. The method was validated through closure, by transferring calibration between three different radars in two different case studies. For the first case, involving three W-band radars, the bias found was of 0.2 dB. In the second case, involving two W-band and one X-band radar, the bias found was of 0.3 dB. These results imply that the biases introduced by performing the calibration transfer with this method are negligible.


KEYWORDS: Cloud retrieval; Data quality control; Radars/radar observations; Weather radar signal processing; Algorithms

1. Introduction

Cloud and precipitation processes occurring in mixed-phase environments are studied with increasing level of priority as their importance covers a broad range of scientific and technical fields. The complex interactions of water vapor, ice crystals, snowflakes, and supercooled liquid water droplets lead numerical weather models to unavoidably simplify the representation of such processes (Rosenfeld and Woodley 2000; Tapiador et al. 2019), which have a very large impact in their final performance (Grabowski et al. 2019). Ice and mixed-phase clouds also present dangerous environments that impact aviation authorities and industries, since it is still hard to evaluate both conceptually and empirically, at the time of design or acceptance of sensitive equipment, the potential risk exposure to these threats (Haggerty et al. 2019; Wang et al. 2012).

Field observations of these cloud types are key to properly assess their physical processes. Yet, such retrievals are usually expensive and hard to gather. This situation motivated the ICE-GENESIS campaign (Billault-Roux et al. 2023), which combined the best available measurement techniques to observe ice and mixed-phase clouds, both in situ and remotely. In this campaign, we highlight the use of one X-band and three different W-band radars retrieving reflectivity, Doppler velocity, and Doppler spectrum observations from the surface. These measurements should prove key in later studies regarding micro- and macrophysical cloud properties, such as their liquid water and ice content, melting-layer height, precipitation rate, and inner cloud turbulence, among others (e.g., Protat et al. 2007; Liao et al. 2009; Trömel et al. 2019).

Radar calibration has an important impact when performing such microphysical retrievals. Errors in the calibration constant value will bias each reflectivity retrieval. For example, a calibration error of 1 dB will bias ice content retrievals by about 15%–20% (Fox and Illingworth 1997; Ewald et al. 2019). However, radar calibration can be difficult to implement. One of the reasons is that, in general, the chosen calibration setup will depend on the specific characteristics of each instrument and on their operating conditions. Along with these technical difficulties, there is also the need to

 Denotes content that is immediately available upon publication as open access.

Corresponding author: Susana Jorquera, susana.jorquera@latmos.ipsl.fr

DOI: 10.1175/JTECH-D-22-0087.1

© 2023 American Meteorological Society. This published article is licensed under the terms of the default AMS reuse license. For information regarding reuse of this content and general copyright information, consult the AMS Copyright Policy (www.ametsoc.org/PUBSReuseLicenses).

reliably estimate calibration uncertainties, which is still an active area of research (e.g., [Chandrasekar et al. 2015](#); [Yin et al. 2019](#); [Toledo Bittner 2021](#)).

Research done at the Centre for Cloud Remote Sensing (CCRES) from the Aerosol, Clouds and Trace Gases Research Infrastructure (ACTRIS) in Europe has provided a two-step calibration strategy. The first step is to select one radar as the reference, and to calibrate it using hard targets such as corner and sphere reflectors ([Yin et al. 2019](#); [Toledo et al. 2020](#)), or distributed targets such as rain ([Hogan et al. 2003](#); [Myagkov et al. 2020](#)). Such methods can be very reliable but are often work intensive and hard to carry out. The second step is to transfer the calibration of the chosen reference instrument to those that are not calibrated, by comparing simultaneous vertical cloud measurements ([Toledo Bittner 2021](#)). The main advantage of the strategy that they propose is that calibration transfer is much simpler to implement, reducing the amount of work that would be needed to calibrate several radars when compared with absolute calibration. In its current implementation it also works between any radar models, as long as they operate in the same frequency band as the reference instrument.

This strategy could prove useful in the context of the ICE-GENESIS campaign, due to the simultaneous use of four different radars at the same site. Yet, the aforementioned methodology must be improved. It is necessary to make the calibration transfer method work even when radars operate in different frequency bands. Also, even though its formulation relies on solid physical and statistical principles, its reliability has not been tested experimentally.

The improvement of current calibration transfer methods would improve the reliability of retrievals taken during the ICE-GENESIS campaign, but the benefits would not be limited to just this. If a validated and reliable multifrequency calibration transfer methodology is put in place, it could represent a valuable asset for existing and future cloud radar networks such as ACTRIS, PROBE, and ARM ([Pappalardo 2017](#); [Cimini et al. 2020](#); [Kollias et al. 2020](#); [ACTRIS 2022](#)). These networks gather cloud measurements from several observatories equipped with X-, Ka-, and W-band radars, distributed at the continental scale. The calibration at each of their sites could be performed with the aforementioned strategy, using a traveling reference radar and a multifrequency calibration transfer methodology. This would help secure the value of such networks, by providing homogenized and comparable data between all their instruments.

The previous antecedents are the motivation for this article. Here we propose significant improvements on previous calibration transfer methodologies ([Toledo Bittner 2021](#)). Physical and technical considerations are made when developing the new algorithms, enabling calibration transfer between different radar models and between radars operating in different frequency bands. This method is tested and validated experimentally using measurements taken during the ICE-GENESIS campaign. Care has been put in presenting the method as an algorithm, to ease its implementation in other observation sites that could require it.

[Section 2](#) describes the ICE-GENESIS dataset and the experimental campaign. [Section 3](#) explains the calibration transfer principle with a review of the requirements and limitations. [Section 4](#) presents the data selection, preprocessing, and data processing to determine the reflectivity data that are comparable to finally estimate the correction coefficient. [Section 5](#) introduces the closure methodology to validate the results exposed in [section 6a](#) for radars of the same frequency band and [section 6b](#) for radars of different bands. [Section 7](#) presents an uncertainty analysis of the method, and [section 8](#) gives the conclusions.

2. Dataset description

Part of the objectives of the international ICE-GENESIS project is to provide comprehensive and reliable observations of snow microphysical properties, to better understand the processes of ice formation in clouds. The properties of interest include crystal size and mass, mass–size relation, fractal dimension, and concentration of snow crystals per volume of air.

To carry out these comprehensive retrievals, it was opted to perform a measurement campaign involving a combination of in situ and remote sensing instruments, both ground based and airborne. The observational campaign was carried out in the second half of January of 2021 at Les Eplatures airport, near the city of La Chaux-de-Fonds in the mountainous region of the Swiss Jura (latitude 47.084877°N, longitude 6.796012°E; altitude 1040 m MSL). This location and season were chosen to maximize the occurrence of snowfall at ground level with little liquid precipitation, to minimize radar attenuation issues, and to make possible low-level flight of the instrumented aircraft to collect in situ data as close to the ground as possible. Additionally, this location is compatible with flights at relatively low altitudes, useful to sample ice in the appropriate temperature range where ice crystal formation occurs (from -10° to $+2^{\circ}$ C) and has the added benefit of enabling the observation and study of orographic induced precipitation processes due to its mountainous surroundings ([Billault-Roux et al. 2023](#)).

A complete list of the instruments deployed in the ICE-GENESIS campaign can be found in [Billault-Roux et al. \(2023\)](#). Since the focus of this study is on cloud radar calibration transfer, we focus the dataset description on the cloud and weather radars involved in the campaign. The ground-based cloud radars were a 95-GHz FMCW Bistatic Radar System for Atmospheric Studies (BASTA) cloud radar named BASTA-mobile ([Delanoë et al. 2016](#)) and a 95-GHz FMCW scanning BASTA named BASTA-mini with the capability to perform hemispherical scans and remain vertically pointing as required in synergy with an 808-nm lidar. The BASTA-mini was calibrated using corner reflectors in 2019 and recalibrated in 2021; a full description of the methodology can be found in [Toledo et al. \(2020\)](#).

In addition to the BASTA cloud radars, a vertically pointing 94-GHz Radiometer Physics GmbH (RPG) Doppler cloud radar ([Küchler et al. 2017](#)) and a 9.42-GHz pulsed weather radar Rain Observation with an X-band Instrument (ROXI; [Lemaître et al. 2016](#)) were located next to the BASTA radars.

TABLE 1. List with the ground-based radars and measurement configuration used for the calibration transfer experiment in the ICE-GENESIS campaign.

Radar	Operating characteristics
BASTA-mini	Vertical max range: 12 000 m Range resolution: 25 m Frequency: 95.82 GHz Time resolution: 1 s Beamwidth: 0.8°
BASTA-mobile	Vertical max range: 12 000 m Range resolution: 25 m Frequency: 94.68 GHz Time resolution: 1 s Beamwidth: 0.4°
RPG	Vertical max range: 10 000 m Range resolution: 7.5/16/32 m Frequency: 94.0 GHz Time resolution: 5 s Beamwidth: 0.48°
ROXI	Vertical max range: 6400 m Range resolution: 50 m Frequency: 9.42 GHz Time resolution: 3 s Beamwidth: 1.86°

The operating characteristics of these four radars are presented in Table 1.

These instruments, continuously collecting data, were separated from each other by less than 10 m, and their measurements were complemented by the MeteoSwiss permanent meteorological site at 500 m from the radar site providing information on surface wind speed, temperature, and precipitation, among others.

In the present study, the simultaneous measurements of reflectivity from each radar will be used to transfer the calibration between each other and to determine the bias between their measurements.

3. Calibration transfer principle

Cloud and weather radars emit an electromagnetic signal capable of interacting with atmospheric hydrometeors such as raindrops, cloud droplets, snowflakes, and ice crystals (Wallace and Hobbs 2006). When the signal reaches these particles, part of its power is scattered backward, toward the radar, where it is ranged and measured. To relate the backscattered power with physical properties of the target, a derived variable defined as the radar reflectivity factor is often used. Equation (1) shows the definition of the radar reflectivity factor in decibel scale (Yau and Rogers 1996; Scolnik 2000):

$$Z(r) = C_z + 2L_{at}(r) + 20 \log_{10}(r) + P_r(r). \quad (1)$$

In this equation, the reflectivity factor $Z(r)$ is calculated using the range r between radar and target, the target backscattered power $P(r)$, the one-way atmospheric attenuation along the signal path $L_{at}(r)$ and a constant term C_z , defined as the radar calibration constant. The units used in this article are dBZ for $Z(r)$, meters

for r , dBm for $P(r)$, dB for $L_{at}(r)$, and $10 \log_{10}(\text{mm}^6 \text{m}^{-5} \text{mW}^{-1})$ for C_z .

Variables r and $P(r)$ are measured directly by the radar; $L_{at}(r)$ can be computed after making some considerations stated further below in this section, and C_z must be obtained from radar calibration (Scolnik 2000; Chandrasekar et al. 2015).

This article provides a methodology to retrieve C_z for an uncalibrated radar by comparing its measurements with those of a collocated reference instrument. For nomenclature purposes, the subindex “ u ” will be included when referring to uncalibrated radar variables. Thus, the uncalibrated radar calibration constant is written as C_{zu} , and its reflectivity measurements are referred to as $Z_u(r)$.

This methodology does not require that both radars operate in the same frequency band. However, some considerations must be made:

- 1) The reference and the uncalibrated radar must observe essentially the same physical phenomena, i.e., the sampling volumes should match, or cloud properties should be uniform enough so that both radars measure the same hydrometeor distribution.
- 2) The scattering regime between the radar signal and hydrometeors must be the same for both radars. When this condition holds, the systematic differences between $Z_r(r)$ and $Z_u(r)$ would only be caused by biases in C_{zu} , and not by differences between each signal scattering function. This condition is always true when comparing same band radars.
When comparing radars that operate in different bands, the identification of hydrometeors for which the scattering regime is the same is not trivial (Nakamura and Inomata 1991). Yet calibration transfer is still possible, if the dataset is adequately selected, and depending on the sampled particles properties (more information in appendix A). The method proposed in this paper deals with both same and different band calibration transfer.
- 3) Attenuation of the radar signal occurs due to electromagnetic energy absorption by the presence of atmospheric gases, and of layers with liquid water (liquid clouds and rain). This attenuation is strongly dependent on the signal wavelength. Meanwhile, ice particles do not introduce significant attenuation at typical cloud radar wavelengths (Matrosov 2009; Tridon et al. 2022). These antecedents have important implications:

- (i) When radars operate in the same frequency band, differences in signal attenuation can be neglected (the term $L_{at}(r)$ is the same for both radars).
- (ii) When radars operate in different frequency bands, differences in signal attenuation due to liquid water presence are not negligible. Therefore, profiles containing only ice cloud samples should be preferred to minimize differences in attenuation.
- (iii) The presence of a liquid water layer over the radome will introduce a bias due to local signal absorption. This loss is usually hard to quantify, and therefore, this situation should be avoided (Germann 1999; Matrosov 2009).

- (iv) In this article, only attenuation due to atmospheric gasses is corrected, using the procedure indicated in [section 4a](#). Ice clouds are identified with the methods mentioned in [section 4b](#).
- 4) Because radar components are not ideal, it is possible to have gain variations introduced by internal radar variables, such as temperature or chirp frequency. These gain variations must be compensated before calibration transfer, to avoid the introduction of biases in the estimated calibration constant value ([Chandrasekar et al. 2015](#); [Toledo et al. 2020](#)).

When these considerations are valid, the systematic difference between reflectivity samples taken with the reference and the uncalibrated radar corresponds to a constant term. This constant is defined as the correction coefficient CC, presented in [Eq. \(2\)](#). It can be observed that a known CC coefficient can be used to correct the uncalibrated radar measurements, rendering them calibrated retrievals ([Toledo Bittner 2021](#)):

$$Z_r(r) = Z_u(r) + CC. \quad (2)$$

The main challenge for calibration transfer, that is, in the estimation of CC, is the identification of data that comply with the aforementioned considerations. [Section 4](#) of this article addresses this challenge by proposing a new methodology to adequately perform such data selection, and to estimate the value of the CC with its uncertainty.

4. Calibration transfer methodology

As stated in the introduction, a direct or naive comparison of collocated data could provide biased calibration results. This section presents a new, comprehensive approach, ranging from data acquisition to postprocessing, that can be used to transfer calibration without introducing biases. The method is conceived to work when transferring calibration between different radar models that may have different sensitivities or may operate in different frequency bands.

To ease the understanding of the methodology, it is divided into four stages, presented in [Fig. 1](#). First, the data collection step consists in preparing an adequate experimental setup with the reference and the uncalibrated radars in place, as indicated in [section 4a](#). These radars then perform simultaneous reflectivity observations.

Second, the data selection and preprocessing ([section 4b](#)) stage takes these raw data and performs a first processing to select cloud periods where calibration transfer could be applied. These selected periods are preprocessed by removing boundary layer data, due to its high inhomogeneity, and by interpolating and collocating reflectivity measurements.

Third, data are processed using a density filter to remove uncorrelated data that may arise from cloud inhomogeneities, differences in radar sensitivity, or noise. The remaining data must pass through a final processing stage to determine the reflectivity range where both radar measurements are within the same sensitivity range, and the same scattering regime ([section 4c](#)).

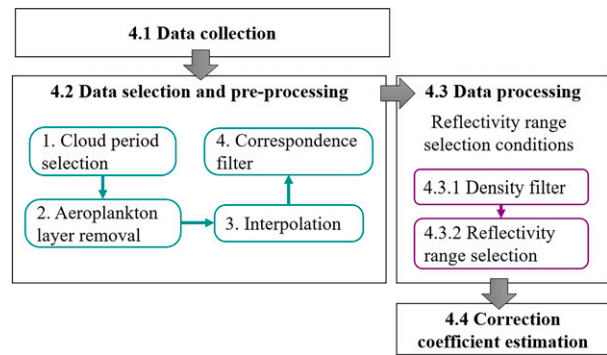


FIG. 1. Calibration transfer flowchart.

Fourth, once the data processing is finished, the CC can be estimated with the procedure presented in [section 4d](#).

Each of these steps is explained in detail in the following sections.

a. Data collection

For a correct application of the calibration transfer method, the two radars, calibrated and uncalibrated, are located in the same place a few meters apart.

When the two radars operate in the same frequency band, the user must be careful to avoid signal interference between the instruments. For our experiment, we tuned the carrier frequency of the BASTA radars several MHz apart from each other and from the RPG signal, as shown in [Table 1](#). The bandwidth of the BASTA radars used is 24 MHz, so the difference is large enough to guarantee no interference, and indeed, no interference was observed. Such verification should be performed prior to initiating any sustained data sampling, including for calibration transfer uses.

After configuration, both radars are left continuously measuring vertical profiles for two weeks [period length suggested by the author [Toledo Bittner \(2021\)](#) based on previous experience].

Signal attenuation due to atmospheric gasses is corrected using [Liebe \(1985\)](#) model. Calculations are done using temperature, pressure, and vapor pressure profiles provided by the ERA5 model taken at the closest coordinate ([Hersbach et al. 2020](#)). This calibration transfer implementation only uses ice cloud profiles, to avoid the impact of cloud liquid water attenuation. The method to identify ice cloud profiles is explained in [section 4b](#).

Some reflectivity samples taken with the BASTA radars are impacted by water deposition on their radomes, because it was not possible to keep them under continuous surveillance. The attenuation introduced by this effect is not negligible. This topic is addressed in [section 6b](#).

b. Data selection and preprocessing

The first step of the method is to select comparable data. This phase is known as data selection and preprocessing and consists of the following 4 steps.

- 1) Cloud period selection: Manual selection of periods with suitable clouds formations for calibration transfer. Following the principles indicated in [section 3](#), cloud profiles with the

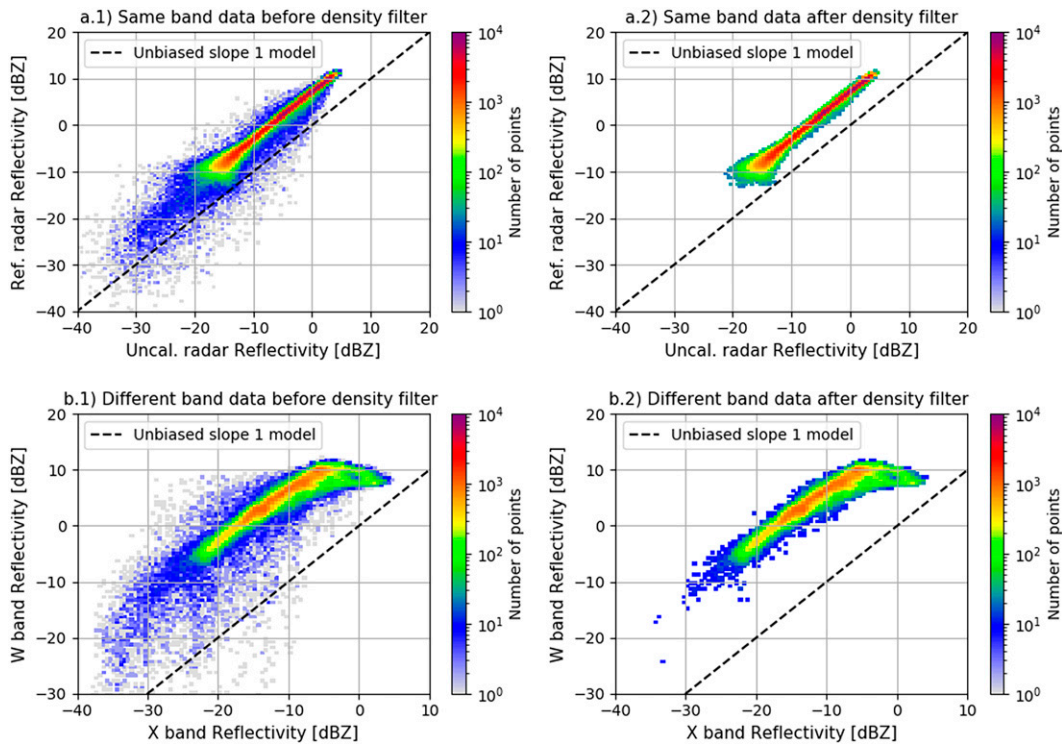


FIG. 2. Example of the density filter application (a.1),(a.2) on same W-band reflectivity data, and (b.1),(b.2) on different W- and X-band data for 2D histograms with (left) the original reflectivity distributions for a given cloud event and (right) the remaining samples after the density filter application for each case.

presence of rain or low-level liquid clouds are removed due to the different impact of liquid particles depending on the radar frequency. Samples taken during periods following rain events are also discarded, because attenuation due to water deposition on the radome is hard to quantify and could introduce biases in reflectivity measurements (Mancini et al. 2018).

Ice clouds are carefully selected by using the radar–lidar synergy. Since liquid and supercooled water can attenuate or even extinguish the lidar signal, the methods proposed by Delanoë and Hogan (2010) and Ceccaldi et al. (2013) are used to identify liquid clouds and supercooled water layers when the environmental temperature is below 0°C. The distinction between supercooled and warm liquid water layers is done using the wet-bulb temperature; if this temperature is greater than 0°C, then is a warm liquid water layer.

- 2) Airborne plankton-layer removal: Removal of the aerial plankton layer by manual inspection. Depending on the environmental conditions, geography, and the season of year, the height of the plankton layer may vary. As the ICE-GENESIS campaign was carefully planned to be carried out in a place with a high tendency to snow in the months of December–February, the environmental temperature was always around 0°C. Under these conditions, the airborne plankton layer does not exist or does not exceed 1000 m height.
- 3) Interpolation: The uncalibrated radar reflectivity data are interpolated to match the reference radar temporal and spatial grid.

- 4) Correspondence filter: All data not detected by both radars are removed. As a result, both radars end with the same amount of coordinated data.

c. Data processing

1) DENSITY FILTER

Ice clouds are usually very homogeneous. Their height also implies that measurements are done at a long range, where the beam is wider. This can help explain why ice cloud profiles taken with radars located a few tens of meters apart tend to be strongly correlated (previous experiences hint that calibration transfer can be done even if radars are a few hundred meters away). Systematic differences in the profiles due to differences in the sampled volume typically become important when observing highly inhomogeneous scattered or short-lived clouds (Toledo Bittner 2021). Apart from cloud inhomogeneities, other sources of uncorrelated measurements are the use of two different radars with unequal sensitivities and signal noise.

To avoid the introduction of systematic biases due to uncorrelated data, we include in the data processing the application of a density filter. This filter has the objective of removing uncorrelated data, including outliers that could bias the calibration transfer. The application of the filter is described next.

First, a 2D histogram comparing data pairs from the reference and uncalibrated radars is made (e.g., Figs. 2a.1,b.1). A

data pair is a collocated pair of reflectivity samples $[Z_r(t_j, r_k), Z_u(t_j, r_k)]$, measured at the same time t_j and distance r_k . Data pairs can always be identified thanks to the previous interpolation step. These histograms are used to assess the repeatability of observed data pairs.

Second, all data corresponding to the less repeated points of the 2D histogram are removed, until reaching 2.5% of the total data. Therefore, the filter removes 2.5% of the collocated data pairs with less repeatability.

Figure 2 illustrates the impact of this filter using data from a calibration transfer exercise on same and different frequency band radars (W band only, and W and X band, respectively). Figure 2a.1 shows the 2D histogram of data before application of the density filter (just after the preprocessing stage) for two radars of the same frequency band. It can be observed that lower reflectivity values tend to be more spread and show a weaker correlation compared with higher values. The Pearson correlation coefficient is 0.98.

Figure 2a.2 shows the resulting 2D histogram after applying the density filter. It can be observed that noisy data have been eliminated due to its lower occurrence rate. This is important because, even if removed data represent a small sample of the total, they can introduce a significant bias in the calculation of the correction coefficient due to their magnitude. The remaining data are highly correlated, reaching a Pearson correlation coefficient of 0.99. The slope is close to 1, especially on the higher reflectivity values (above -10 dBZ on the x axis). Lower reflectivity values do not follow as clearly this slope due to differences in radar sensitivities (between -21 and -12 dBZ approximately). This issue is addressed in the next step of the method [section 4c(2)].

Figure 2b.1 shows unfiltered data for two radars that operate in different frequency bands. Data spread becomes more apparent, especially for reflectivity values under -20 dBZ. This behavior is likely caused by important differences in sensitivity and in scattering regimes. The Pearson correlation coefficient before density filter is 0.88.

After applying the density filter the Pearson correlation coefficient improves reaching 0.92. Yet, Fig. 2b.2 shows that there are areas of high point density where the relationship between the data of both radars does not have a slope of 1 at the higher reflectivity range (above approximately -10 dBZ). This slope deviation is due to the measurement of consistently different reflectivity values, caused by differences in each signal scattering regime.

Other deviations from the unbiased slope-1 model remain for lower reflectivity values (under -25 dBZ on the x axis), due to sensitivity differences. The density filter is not adapted to remove these points, which makes it necessary to apply the reflectivity range selection algorithm explained in the next section.

2) REFLECTIVITY RANGE SELECTION

As introduced in section 4c and in Fig. 2, it may be possible to find highly frequent measurement pairs that do not behave following the slope-1 linear relationship of Eq. (2). This is usually the case when one or more of the considerations indicated in section 3 do not hold, often due to differences in

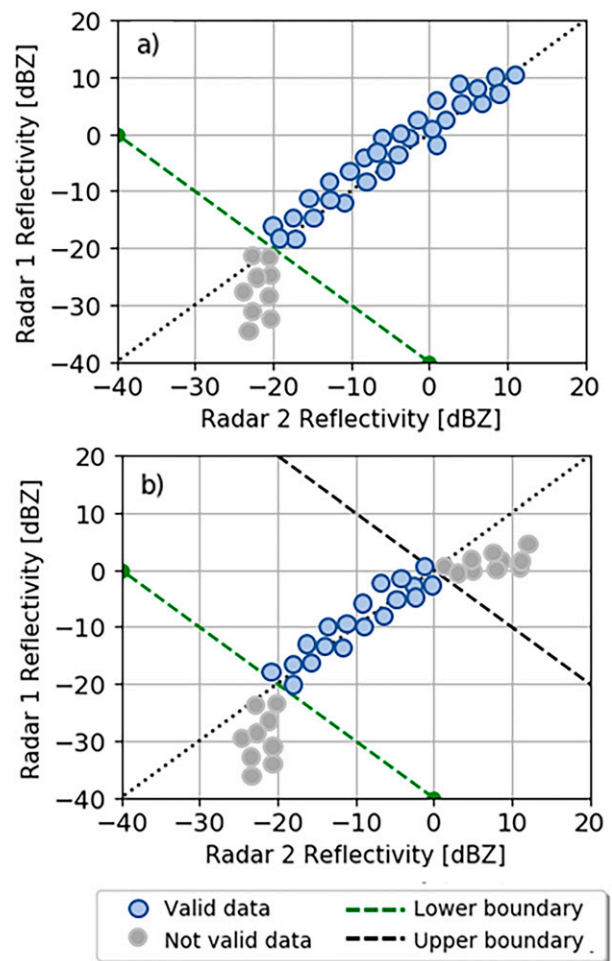


FIG. 3. Scheme explaining the reflectivity range selection concept, using hypothetical data points: (a) How the reflectivity range selection is done for radars of the same frequency band. The green segmented line represents the single lower boundary of reflectivity values, and the comparable data are shown in blue. (b) The reflectivity range selection for radars of different frequency band. In this case a lower (green) and the upper boundary (black) are used. The comparable data are represented by the blue dots.

radar sensitivities or scattering regime. A comparison including these data would bias the final calibration result; hence, it should be filtered.

Fortunately, these effects are strongly dependent on identifiable reflectivity ranges, potentially enabling the implementation of a data filter to remove them. The automatic reflectivity range selection algorithm presented in this article is our proposed solution for the aforementioned task.

For radars operating in the same frequency band, scattering regime and atmospheric absorption differences are negligible. In consequence, the main source of systematic differences in their measurements arises from different instrumental sensitivity, for example, due to different antenna sizes, or the use of different electronic components. Figure 3a shows an example on how hypothetical reflectivity data would appear in this

situation. In this example, values between -20 and approximately 10 dBZ have a behavior very close to a straight line with slope 1, since both instruments operate at the same scattering regime. Meanwhile, when reflectivity values reach less than -20 dBZ, Radar 2 is no longer sensitive to signal changes at the same time that Radar 1 retrievals reach down to -35 dBZ. This situation has been observed with real measurements. For example, Toledo Bittner (2021) observed that not taking into account sensitivity differences between a BASTA-mini and an RPG cloud radar could introduce a bias of up to 6 dB in the correction coefficient estimation. Therefore, it becomes necessary to identify the lower boundary of the reflectivity range where both radars are sensitive to measurement changes, indicated by the green line in Fig. 3a, before performing calibration transfer using these hypothetical data.

Reflectivity retrievals sampled with two radars of different frequency bands can have systematic differences due to variations in atmospheric and cloud signal absorption, scattering regimes, and instrument sensitivities. The method to mitigate the impact of atmospheric and cloud signal absorption is explained in section 3. The remaining effects introduce the behavior shown in Fig. 3b. As in the same band case, lower reflectivity values are impacted by sensitivity differences, skewing data away from the slope 1 that would be obtained under ideal conditions.

Meanwhile, differences in signal scattering introduce a deviation from the slope 1 in the higher reflectivity range. This deviation appears because, for larger hydrometeors, the radar with the shorter wavelength enters the Mie scattering regime before the one with the longer wavelength. This departs from the ideal radar equation behavior, and thus, reflectivity estimates become biased by a different amount for each instrument. This regime has been observed, for example, when comparing W- and X-band measurements. The W-band radar tends to underestimate reflectivity values with respect to the X band for larger hydrometeors. A study on this subject using real ice cloud data is presented in the appendix A. This effect has also been observed by Nakamura and Inomata (1991). They found differences in reflectivity retrievals of up to 5 dB between Ka- and X-band reflectivities when comparing rain observations, caused by differences in the scattering regime at each radar band.

Attenuation and scattering effects when comparing different band radars make it necessary to define two boundaries, as shown in Fig. 3b. First, the lower reflectivity boundary to avoid biases due to differences in the radar sensitivities, as in the same frequency band case. Second, a new boundary identifying where the scattering regime becomes different between the radars, a phenomena observable as a depart from the slope-1 trend, drawn in this illustration as a black line passing through 0 dBZ. Thus, comparable data remain between the green and black segmented lines (blue dots).

Several authors have proposed methods to find the most suitable reflectivity range for calibration transfer. Toledo Bittner (2021) proposes a method based on comparing the dynamic range in power measurements of a reference and uncalibrated radar. The use of this method is limited since it is only applicable to radars of the same frequency and requires raw measurements of

the radar received power. Hogan et al. (2000) proposed another method based on defining a reflectivity threshold where cloud samples would always be in the Rayleigh regime. This method is not recommended because the threshold value depends on the frequency of each radar, and therefore, it is hard to generalize (Battaglia et al. 2020). Other authors propose to select cloud portions where ice particles predominate, i.e., cloud top, reducing the effect of different scattering regimes (Tridon et al. 2020).

To define an appropriate reflectivity range, in this paper we propose an iterative process that evaluates several score parameters for different reflectivity ranges. The data in the selected reflectivity range must minimize the difference between their slope and the value of 1, maximize their coefficient of determination R^2 with respect to a linear model, not surpass 40% of data discarded, and minimize the root-mean-square error (RMSE) between data and the best fit of an unbiased slope-1 model. To simplify the reading of this article, a detailed description of the reflectivity range selection methodology is presented in appendix B.

d. Correction coefficient estimation

Equation (2) shows how the uncalibrated data can be corrected when the CC is known. This section describes how its value and uncertainty using one or more cloud events.

First, a correction coefficient per period K_i is calculated for each cloud event i (dB), then K_i is calculated using the mean of the reflectivity values for each radar [Eq. (3)]. The standard deviation σ_{K_i} is later used when calculating the CC uncertainty:

$$K_i = \text{mean}(Z_{\text{cloud}_i}^{\text{ref}} - Z_{\text{cloud}_i}^{\text{uncal}}) \quad \text{and} \quad (3)$$

$$\sigma_{K_i} = \text{SD}(Z_{\text{cloud}_i}^{\text{ref}} - Z_{\text{cloud}_i}^{\text{uncal}}). \quad (4)$$

Then, the uncertainty associated with each K_i estimation is calculated as

$$\delta K_i = \sqrt{\frac{1}{M_i} \sum_j^{T_i} \sum_k^{R_N} (K_i^{jk} - K_i)^2}. \quad (5)$$

Here, the term T_i represents the number of reflectivity profiles retrieved in the time period i , with R_N being the number of range gates; $M_i = T_i R_N$ represents the number of valid reflectivity samples in the same period, and K_i^{jk} is the correction coefficient calculated using individual reflectivity samples, taken at a time t_j and at a distance r_k :

$$K_i^{jk} = Z_{\text{cloud}_i}^{\text{ref}}(t_j, r_k) - Z_{\text{cloud}_i}^{\text{uncal}}(t_j, r_k). \quad (6)$$

The CC is estimated as the mean of all the K_i values sampled from the total number of cloud events N :

$$\text{CC} = \frac{1}{N} \sum_{i=1}^N K_i. \quad (7)$$

The uncertainty in the CC estimation is calculated using Eq. (8). Here, σ_{ref} represents the reference radar calibration uncertainty, σ_K is the standard deviation of the K_i coefficients used

to calculate the CC, and σ_{K_i} is the standard deviation associated with each K_i calculation [see Eq. (4)]:

$$\delta\text{CC} = \sqrt{\sigma_{\text{ref}}^2 + \frac{(\sigma_K)^2}{N} + \left(\frac{1}{N^2} \sum_{i=1}^N \sigma_{K_i}^2\right)}. \quad (8)$$

Equation (8) shows that use of a larger number of cloud events should contribute to decreasing the uncertainty of the CC estimation, improving its reliability. A study on the behavior of δCC using real measurements is presented in section 7.

5. Closure methodology

The objective of the methodology described in section 4 is to provide an unbiased estimation CC [Eq. (7)]. To validate that the methodology achieves this objective, a closure approach is used.

The calibration transfer closure is tested using three different radars, henceforth named Radar 1, Radar 2, and Radar 3. A correction coefficient is calculated for each radar pair using the methodology of section 4. This provides three correction coefficients: $\text{CC}_{\text{radar1}-\text{radar2}}$ when Radar 1 is used as reference and Radar 2 as uncalibrated, $\text{CC}_{\text{radar2}-\text{radar3}}$ when Radar 2 is the reference and Radar 3 is uncalibrated, and $\text{CC}_{\text{radar3}-\text{radar1}}$ when radar 3 is used as a reference to calibrate radar 1. The use of these three correction coefficients with successive applications of Eq. (2) provides the relationship

$$\begin{aligned} Z_{\text{radar1}} &= Z_{\text{radar2}} + \text{CC}_{\text{radar1}-\text{radar2}} \\ &= Z_{\text{radar3}} + \text{CC}_{\text{radar2}-\text{radar3}} + \text{CC}_{\text{radar1}-\text{radar2}} \\ &= Z_{\text{radar1}} + \text{CC}_{\text{radar3}-\text{radar1}} + \text{CC}_{\text{radar2}-\text{radar3}} \\ &\quad + \text{CC}_{\text{radar1}-\text{radar2}} \\ &= Z_{\text{radar1}} + R. \end{aligned} \quad (9)$$

The residual R is defined as

$$R = \text{CC}_{\text{radar1}-\text{radar2}} + \text{CC}_{\text{radar2}-\text{radar3}} + \text{CC}_{\text{radar3}-\text{radar1}}. \quad (10)$$

It can be observed that the relationship of Eq. (9) is only valid if $R = 0$. This condition is equivalent to stating that closure is achieved without introducing a bias, since successive calibration transfers between different radars would provide the same final reflectivity measurements. On the contrary, if there was a systematic bias in the method, the value of R would be different than zero. Therefore, the calculation of R provides a way to evaluate if there is a bias in the method through closure.

When calculating R it is important to consider that correction coefficients estimated from experimental data have an associated uncertainty (section 4d). The propagation of these uncertainties enables the calculation of the total uncertainty in R , which is also a necessary value when assessing the experimental results.

The next section presents the results of two closure experiments. The first used three W-band radars, and the second two W-band and one X-band radar. The correction

coefficients CC, residual R , and its uncertainty are calculated and discussed.

6. Closure results

a. Case 1: Calibration transfer on radars with the same band

This section presents the results of the calibration transfer and closure between three radars of the same frequency band. The data used correspond to the period between 1000 and 1900 UTC 16 January 2021 at Les Eplatures airport. On this day, no rain or snow was observed in the previous hours, the radomes of the BASTA radars were clean, and the surface temperature was less than 0°C throughout the day.

Figure 4 shows the reflectivity measured by BASTA-mini (Fig. 4a.1), BASTA-mobile (Fig. 4a.2), and RPG (Fig. 4a.3) radars simultaneously. The observed cloud is most likely made of ice particles, due to its high reflectivity values and the low surface temperatures. It can be observed that the higher sensitivity of the RPG radar enables to observe cloud features undetected by the other instruments (at approximately 8 km of range). Most of these data are filtered before the comparison at the preprocessing stage, during interpolation and application of the correspondence filter (section 4b).

The next step is shown in the second line of Fig. 4. Here, Figs. 4b.1–b.3 show 2D histograms of collocated reflectivity data for each radar pair, before data processing (more precisely, after data preprocessing and before the density filter, see Fig. 1). Figure 4b.1 shows BASTA-mini and BASTA-mobile data. It can be seen that the radars have very similar sensitivities and that there is a high concentration of points around the unbiased slope-1 model. Yet, at this stage, data are still noisy and show areas of low correlation. Meanwhile, Fig. 4b.2 shows the 2D histogram of collocated reflectivity data for BASTA-mobile and the RPG radar, and Fig. 4b.3 for the RPG radar and the BASTA-mini. These figures also have areas where measurements have low correlation, especially for low reflectivity values (≤ -15). In Fig. 4b.3 it is possible to observe some impact of sensitivity differences for the lower reflectivity values, observable as an asymmetry around the main data axis of slope 1 (between -25 and -30 dBZ as measured by the BASTA-mini).

Figures 4c.1–c.3 show the result after all data processing (notably after the reflectivity range selection). It can be observed that low correlation and noisy data have been removed. In all 3 cases the slope of the selected data is very close to 1. The selected data portion is sufficiently representative since it covers a reflectivity range of at least 20 dB, and at least 60% of the original samples remain used for the 3 cases.

Table 2 shows the calibration transfer results for this single period. It is observed that systematic differences in reflectivity samples between the different radars can reach up to 3.9 dB, a value retrieved when transferring the calibration between BASTA-mobile and RPG radar. Meanwhile, the lower correction value of 1.5 dB corresponds to the difference between the BASTA-mini and the BASTA-mobile. This smaller difference is probably explained by the fact that both radars are

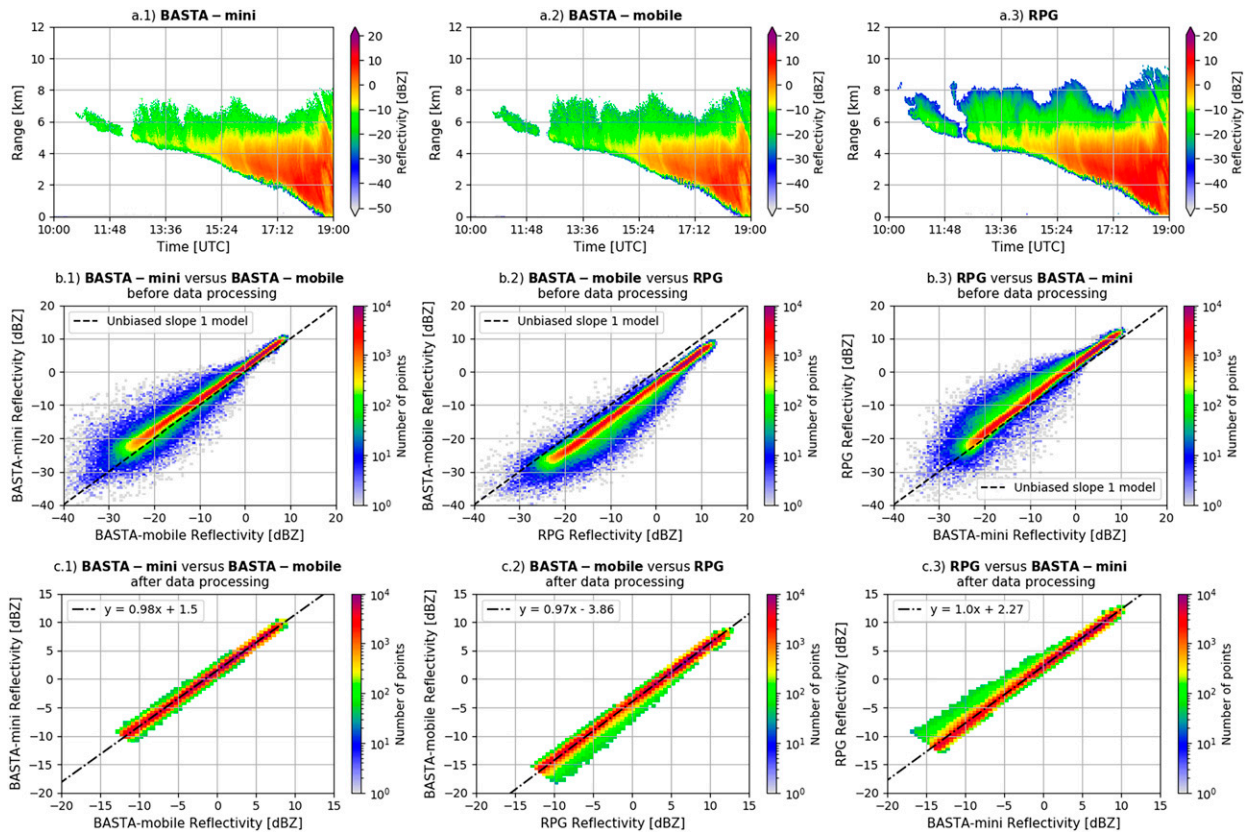


FIG. 4. Reflectivity measurements on 16 Jan 2021 for three radars operating in the W band: (a.1)–(a.3) The same phenomenon observed by each radar. (b.1)–(b.3) A 2D histogram of the reflectivity before data processing. (c.1)–(c.3) The result of the selection of the reflectivity range.

supplied and calibrated by the same manufacturer. For all cases, uncertainty in the retrieved correction coefficients remains under 1 dB.

To evaluate the unbiasedness of the method, we now calculate the residual R introduced in Eq. (10). Its result is presented at the end of Table 2. Its resulting value of $R_{\text{case1}} = -0.2 \pm 1.1$ dB is consistent with an unbiased calibration transfer method, and therefore, we can conclude that closure is valid for this experiment.

b. Case 2: Calibration transfer on radars with different band

The second case deals with calibration transfer between radars of different frequencies. It involves a BASTA-mini and

an RPG radar, which operate in the W band, and the ROXI radar, which operates in the X band. The data correspond to the period between 0300 and 0400 UTC 27 January 2021.

Figure 5a.1–a.3 show the reflectivity measurements for BASTA-mini, ROXI, and RPG, respectively. It can be observed that BASTA-mini reflectivity data are shifted toward significantly lower values compared to the other radars measurements. This shift is caused by snow deposition on the instrument radome, happening during the previous day. Since the radar box is heated, the radome interface may melt some of this snow producing liquid water that contributes to attenuating radar measurements. Even though a wet radome is not optimal for calibration transfer, results show that this effect is constant enough in the time window analyzed to not introduce systematic shifts in the retrieved correction value, even though it would only be valid for measurements taken under these exact physical conditions. Since the objective is only to verify the closure of the calibration transfer method, the radome conditions are not considered as an issue. In fact, calibration transfer in this case could be used to correct the radar measurements an get valid physical retrievals from BASTA-mini this day based on another instrument. For example, the bias in the RPG measurements due to snow cover is expected to be smaller or negligible, since this instrument has a blower to prevent deposition of liquid or solid precipitation particles on the antennas.

TABLE 2. Calibration transfer results under clean radome conditions, for radars with the same frequency band.

Radars compared	CC (dB)	Percentage of accepted samples
$Z_{\text{RPG}} - Z_{\text{BASTAmini}}$	2.2 ± 0.7	73.9%
$Z_{\text{BASTAmini}} - Z_{\text{BASTAmobile}}$	1.5 ± 0.5	74.3%
$Z_{\text{BASTAmobile}} - Z_{\text{RPG}}$	-3.9 ± 0.7	71.8%
R_{case1}	-0.2 ± 1.1	

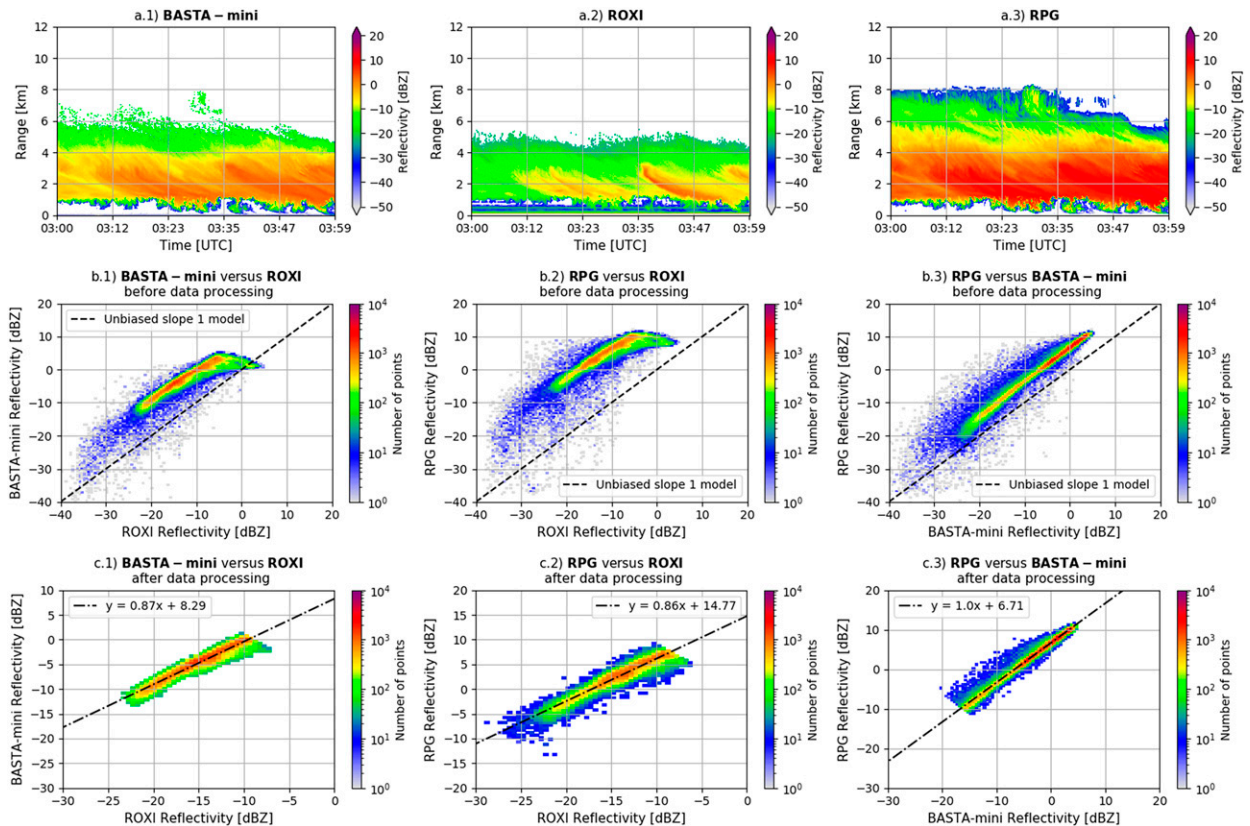


FIG. 5. Reflectivity measurements on 27 Jan 2021 for three radars, BASTA-mini and RPG in the W band and ROXI in the X band: (a.1)–(a.3) The same phenomenon observed by each radar. (b.1)–(b.3) A 2D histogram of the reflectivity before data processing. (c.1)–(c.3) The result of the selection of the reflectivity range.

Another interesting observation is the lower sensitivity of ROXI for particles above 4 km of height, compared with W-band radars, even though atmospheric attenuation is stronger in the W band (Liebe 1989). This effect can be explained by differences in the radars scattering regime. The shorter wavelength of W-band radars (~ 3 mm) enables them to interact in Rayleigh scattering regime for smaller particles with respect to X-band radars (wavelength of ~ 3 cm). Indeed, for small cloud droplets or ice crystals, it is possible to have situations where the X-band radar has a negligible scattering (Wallace and Hobbs 2006). Therefore, this sensitivity difference can also be used as an indicator of the presence of smaller ice crystals with respect to particles below ~ 4 km.

Figure 5b.1 shows a 2D histogram with the distribution of reflectivity measurements taken with the BASTA-mini and ROXI radars, before data processing. A strong correlation of the data can be seen in a nonnegligible portion of the reflectivity range; however, less correlated data are also observed for low reflectivity values (under approximately -10 dBZ on the BASTA reflectivity scale). For higher reflectivity values, it can be seen that the data remain highly correlated, but with a slope that departs from the slope-1 line (above ~ 5 dBZ on the BASTA reflectivity scale). This behavior is also observed between ROXI and RPG in Fig. 5b.2, above approximately -8 dBZ on the RPG scale. This indicates that measurements

were taken when both radar signals were under different scattering regimes. As explained in sections 3 and 4, these measurements must not be taken in consideration when calculating the calibration correction coefficient.

Figures 5c.1–c.3 show 2D histograms of the reflectivity data after the complete data processing chain. It can be observed that uncorrelated data have been removed, as well as data that strongly departed from the unbiased slope-1 linear relationship between measurements. When comparing different frequency bands, in Figs. 5c.1 and 5c.2, it is more difficult to reach the slope-1 condition while maintaining a percentage of accepted samples above 60%; hence, slopes are slightly lower and results have a larger uncertainty, as shown in Table 3.

Table 3 shows the calibration transfer and closure results. Indeed, the calibration transfer uncertainty between radars of

TABLE 3. Intercomparison results, for radars with different frequency band.

Radars compared	CC (dB)	Percentage of accepted samples
$Z_{\text{RPG}} - Z_{\text{BASTAmini}}$	6.7 ± 0.7	83.9%
$Z_{\text{BASTAmini}} - Z_{\text{ROXI}}$	10.3 ± 1.0	65.5%
$Z_{\text{ROXI}} - Z_{\text{RPG}}$	-16.7 ± 1.2	65.2%
R_{case2}	0.3 ± 1.7	

different band increases when compared with same band calibration transfer (1.0 and 1.2 dB versus 0.7 dB for the same band case). Meanwhile, the same band case uncertainty is consistent with the values found in case 1.

When testing closure, the found residual is of $R_{\text{case2}} = 0.3 \pm 1.7$. The result is very close to 0, as expected in an unbiased calibration experiment, yet uncertainty remains relatively high. We conclude that this result indicates that the method is highly likely to be unbiased, at least within 1.7 dB of uncertainty, but possibly much less. The main sources of uncertainty arises in this calculation from the comparison of different band due to possible contributions of particles under different scattering regimes that may remain despite imposing a slope close to 1 between in data comparison, and could also be influenced by the radome state and atmospheric attenuation.

7. Uncertainty analysis

Previous results show that calibration transfer accuracy can be improved by combining observations from several independent cloud events (Toledo Bittner 2021). This improvement is observed as a successive reduction of the calibration transfer uncertainty following the number of comparisons, until reaching a convergence at a lower value with respect to a single case.

To test if we replicate this result with our new method, we identify 9 suitable cloud periods observed by both BASTA-mini and BASTA-mobile between December 2020 and January 2021. Equation (8) is used to calculate the uncertainty in the CC estimation when increasing the amount of cloud periods used in its calculation. The results are shown in Fig. 6.

Figure 6 shows that if only the first period is used to determine a final correction coefficient, the uncertainty exceeds 1 dB. This value decreases down to 0.5 dB when more periods are included.

In addition, when comparing the result using 9 periods with what is stated in Table 2, it can be observed that the estimated bias between BASTA-mini and BASTA-mobile differs by 12%.

These results show that a single cloud period can already provide an estimation of the calibration coefficient. However, if additional reliability or less uncertainty is needed, it is advisable to consider several periods in the correction coefficient calculation. The use of more cloud periods will also remove possible biases that could be introduced by the use of a single cloud observation.

8. Conclusions

This article presents a new calibration transfer methodology that is applicable for cloud radars of both the same and different frequencies. This method consists in comparing reflectivity profiles retrieved with a reference radar with those observed by an uncalibrated radar, to determine a correction coefficient for the uncalibrated instrument. Ice cloud profiles are preferred in the current implementation, because they enable the neglect of microwave absorption by liquid water, which is difficult to quantify based solely on radar measurements. The approach has been developed using measurements from the ICE-GENESIS campaign, involving three

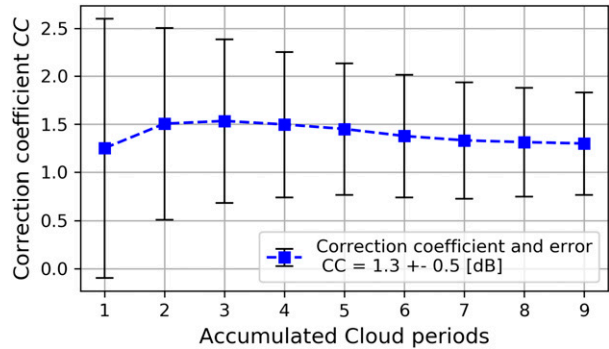


FIG. 6. Correction coefficient CC calculated with an increasing number of cloud periods. These nine periods were observed between December 2020 and January 2021 and have a combined sampling duration of 53 h.

collocated W-band radars and one X-band radar. Its validation is done by closure by doing successive calibration transfer between the instruments, taking advantage of the presence of several radars on site.

The method consists on several steps. First, ice cloud profiles are retrieved simultaneously using the two collocated radars. Second, an identification of periods with comparable targets is manually done. Specifically, we search for ice cloud profiles without liquid water or precipitation. Third, a data selection stage (density filter) is used to remove noncorrelated data between the radars, which may be produced by differences in the radar sensitivities, in the sampling volumes or by signal noise. Fourth, a valid reflectivity range selection is performed to only include data that sampled under the same scattering regimes. This step is especially important when comparing different band radars, since systematic differences are expected when comparing measurements done at different bands, for some reflectivity ranges. If this effect is left unchecked, it may bias the correction coefficient estimation. These reflectivity range selection is done by comparing data with a slope-1 linear model used as a reference. Finally, the correction coefficient is obtained by adjusting this model with the remaining, comparable data.

The found correction coefficients for radars of the same frequency band were between 2.2 and -3.9 dB, with uncertainties on the order of 0.7 dB. The difference of 2.2 dB found between BASTA-mini and the RPG radar is probably caused by manufacturers using different calibration methods. Meanwhile, for radars with different frequencies the correction coefficient reached values between 10.3 and -16.7 dB with an uncertainty on the order of 1 dB. These large values are mostly explained by snow accumulation on the radomes or antennas. When comparing different band radars the uncertainty is higher, but the closure results show that the result remains statistically unbiased. It is worth noting that the uncertainty in the calibration transfer method must be added to the reference radar calibration uncertainty to determine the total uncertainty of the newly calibrated radar.

The validation of the method is done by closure, by performing a closed calibration transfer loop with three radars.

The calibration transfer bias is calculated by adding all the correction coefficients obtained. Results show a bias of 0.2 dB for radars of the same band, and of 0.3 dB for radars of different bands. Its value is significantly smaller than the uncertainty associated with each estimated correction coefficient, indicating that the introduced bias is negligible.

Calibration transfer using several cloud cases also shows promising results. The absolute correction coefficient value showed a variability of 0.3 dB when comparing results from 9 different cases. Uncertainty in the correction coefficient also decreased when increasing the number of cloud cases used. This result shows that it is possible to refine the calibration transfer accuracy if an application requires it, by increasing the number of sampled cloud cases.

In conclusion, the new calibration transfer methodology is validated and can be applied with confidence for same and different band cloud radars, at least between the X- and W-band range. Its flexibility and relatively ease of implementation enables its use during measurement campaigns, or for the calibration of more durable observation stations in radar networks. It requires a calibrated reference instrument, but without other specific technical needs (such as brand or frequency band), as long as both are sensitive enough to measure reflectivity from ice clouds.

Future improvements of calibration transfer methodologies should focus on situations when the instruments are not collocated, for example for airborne or satellite-based radars. Most of the principles included in this article should remain valid and directly applicable. Aircraft based radars are highly relevant for campaigns such as ICE-GENESIS, due to the amount of additional information they can provide when combined with in situ instruments, and therefore, future developments are foreseen in this direction (Protat et al. 2007; Wang et al. 2012). The calibration and verification of satellite-based radars is also of special interest, since they provide a large number of measurements distributed around the globe (e.g., Protat et al. 2009). In addition, satellite-based radars could also be used to calibrate radars installed at remote locations, without transporting a ground-based reference instrument next to an uncalibrated one, through two successive calibration transfer operations.

Acknowledgments. We thank the entire team that participated in the ICE-GENESIS project and the BASTA team Christophe Le Gac, Jean-Paul Vinson, Christophe Caudoux, Fabrice Bertrand, and Nicolas Pauwels from the LATMOS laboratory for their technical support. We acknowledge the Center for Cloud Remote Sensing (CCRES) of the ACTRIS research infrastructure for providing time and technical support that helped in improving the quality of this article. The funding from the European Union's Horizon 2020 research and innovation program under Grant Agreement 824310 is gratefully acknowledged. We also thank the reviewers for their dedicated and detailed comments, which were of great help in improving the quality of the article.

Data availability statement. The entire dataset obtained during the ICE-GENESIS campaign is available on the Aeris website (<https://ice-genesis.aeris-data.fr/catalogue/>).

APPENDIX A

Theoretical Relationship Between X- and W-Band Reflectivity for Ice Particles

High Altitude Ice Crystals (HAIC; [Dezitter et al. 2013](#)) was a European project that was primarily designed to collect statistics on the levels of total water content and ice crystal sizes in high ice water content regions of mesoscale convection to support the assessment of a new ice crystal icing aircraft certification envelope for ice crystals ([Leroy et al. 2017](#)).

During this project, two measurement campaigns were carried out. The first in Darwin in northern Australia, 2014 and the second in Cayenne, French Guyana, 2016. The data were taken on board the F20 French research SAFIRE airplane whose objective was to get as close as possible to convective zones. The plane was equipped with the RASTA radar and in situ measuring instruments to study the microphysical properties of highly concentrated ice crystals ([Haggerty et al. 2019](#)).

To study the feasibility of applying the calibration transfer method between radars of different bands, it is necessary to verify that there are realistic conditions in which such instruments could operate simultaneously in the same scattering regime. To test this requirement, we study the equivalent radar reflectivity of real ice particles, sampled during the HAIC campaigns using airborne particle counters flown through ice clouds. Since the article compares measurements from radars in the X and W bands, we calculate reflectivity for these two ranges using the T-matrix method ([Leinonen 2014](#); [Mishchenko and Travis 1994](#); [Mishchenko et al. 1996](#); [Wielgaard et al. 1997](#)). As is mentioned in the article text, when calibrating radars it is important to avoid the presence of liquid clouds because they would introduce a bias due to different attenuation intensity in different bands. Therefore, it is decided to consider particles registered with temperatures under -1°C only. We decided to use these data and not the data collected during the ICE-GENESIS field campaign so as to cover a much wider range of temperature and particle size.

This calculation provides the results of [Fig. A1](#). Here, [Fig. A1a](#) shows the statistical behavior of X- versus W-band reflectivities for real ice particles, and a curve with the mean of W-band reflectivity for each X-band value. [Figure A1b](#) shows the slope of the mean curve of [Fig. A1a](#), and [Fig. A1c](#) shows its difference with respect to the slope-1 model.

It can be observed that, between -25 and 5 dBZ approximately, there is a regime where the mean behavior of both radar reflectivities is proportional and very close. [Figure A1b](#) shows that the slope in this reflectivity range is within 0.9 and 1.0, and [Fig. A1c](#) shows that the mean bias in this range is less than 0.5 dB.

Conversely, for reflectivity values above 5 dBZ, X-band reflectivity increases faster than for the W band. This difference happens because higher reflectivity values are associated with larger ice crystals, which become closer in size

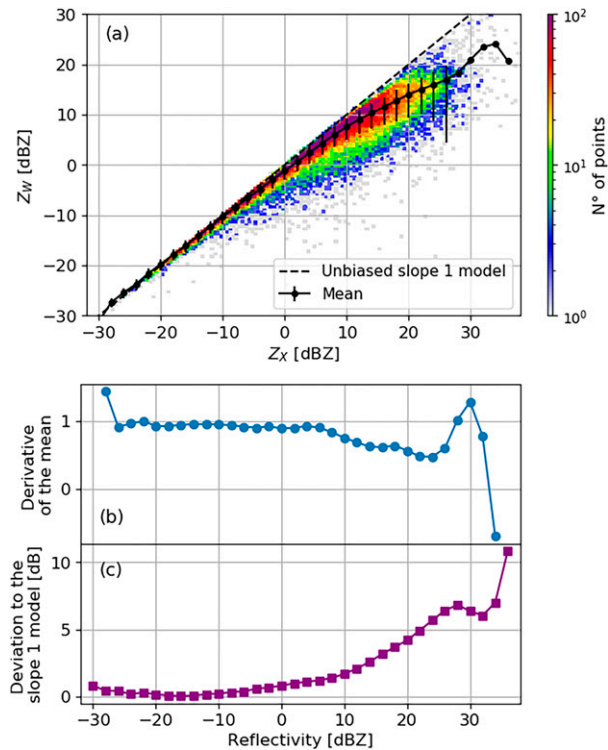


FIG. A1. (a) HAIC reflectivity data for W band and X band. The black dotted line corresponds to the reflectivity mean. (b) Slope of the reflectivity mean. (c) The deviation of the reflectivity mean with respect to the unbiased slope-1 model.

with the smaller wavelength of the W band (~ 0.3 cm) (Wallace and Hobbs 2006). Therefore, the W-band radar enters the Mie scattering regime before X-band radars, which have a longer wavelength (~ 3 cm). Since Mie backscattering is weaker than Rayleigh, the slope in Fig. A1b decreases abruptly until approximately 20 dBZ. Thus, the mean bias, in Fig. A1c, increases due to the different scattering regimes in each band. The curves above 20 dBZ become unreliable, most likely due to more variability in the scattering regimes, the increased importance of shape ratio for larger particles, and the lesser amount of data available.

The analysis of this section shows that it is possible to find realistic conditions under which both radar bands would interact with the hydrometeors in the Rayleigh regime. It also shows that in these conditions, the mean bias would be smaller than 0.5 dB, and that the correlation of the measurements should be very close to 1. These conditions are preferable and therefore should be identified to perform calibration transfer between radars on different bands.

APPENDIX B

Reflectivity Range Selection Methodology

To apply the reflectivity range selection methodology, it is necessary to first perform the procedure exposed in section 4b.

In this way both radars get the same grid of valid reflectivity data, necessary for the next steps of this method. At this stage, it is also advisable to plot a 2D histogram or heatmap of the case under study to get an overview.

The reflectivity range selection methodology is described as follows.

1) Unbiased slope-1 model: A theoretical model line with slope 1 is defined and fitted to the data. This model is based on the relationship expressed in Eq. (2). The line model is used as a reference to compare the behavior of the actual data. The next step depends on whether radars operate in the same or different frequency band. *If radars are in the same frequency band*, then selection of the data portion is done for each iteration i . The objective is to find the data portion that fits better to the unbiased slope-1 model:

- A line of slope -1 is defined as a lower boundary i to delimit the minimum of the reflectivity range for the current iteration i . For the iteration $i = 0$ the line is defined according to the minimum reflectivity collocated pair as indicated in Fig. B1a.
- A line of slope -1 is defined as upper boundary to delimit the maximum of the reflectivity range. This line is the same for each iteration and is defined according to the maximum reflectivity collocated pair.

If radars are in different frequency bands, then selection of the data portion is done for each iteration i, j :

- A line of slope -1 is defined as a lower boundary i to delimit the minimum of the reflectivity range for the current iteration i . For the iteration $i = 0$ the line is defined according to the minimum reflectivity collocated pair as shown in Fig. B1c.
- A line of slope -1 is defined as upper boundary j to delimit the maximum of the reflectivity range. For the iteration $j = 0$ the line is defined according to the maximum reflectivity collocated pair.

2) Comparison of the data selection with the unbiased slope-1 model: The portion of data between the boundary lines for each iteration (i, j) is used to evaluate the data and compare them with the unbiased slope-1 model using the coefficient of determination R^2 , the real slope of the data, the percentage of the data and the RMSE.

3) Change in upper boundary j , iteration in the line delimiting the maximum: The upper boundary moves by 2 dB, covering a smaller portion of the data. While the lower boundary remains the same. See Fig. B1d example of iteration for radars of different band where upper boundary was moved. For same frequency radars the upper boundary remains as in the iteration $i = 0$ always at the same position, see Fig. B1c. The iterations in the upper boundary are performed repeating step 3 and 4 until both boundary lines are separated by 2 dB.

4) Change in the lower boundary i , iteration in the line delimiting the minimum: The lower boundary moves by 2 dB reducing the portion of the data. See Fig. B1b example of iteration for radars of the same band and Fig. B1d for radars of different band. Then step 4 is repeated.

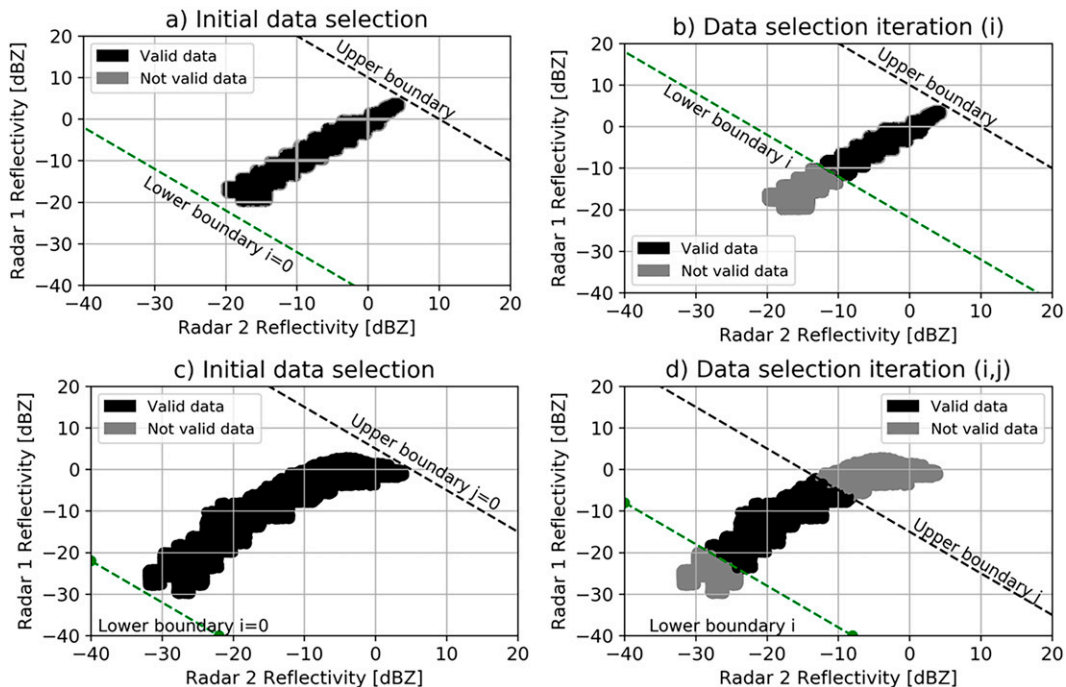


FIG. B1. Reflectivity range selection. (a) The data selection for the first iteration for radars of the same frequency band. (b) The data selection for the iteration i . Iterations with radars of the same band are performed by changing only the lower boundary. (c) Data selection for the first iteration when comparing with radars of different frequency band. (d) Data selection for the iteration i, j when comparing with radars of different frequency band. The iterations are performed by changing both lower boundary and upper boundary.

- 5) Accepted iterations: The accepted iterations are those that satisfy simultaneously the criteria of the coefficient of determination R^2 within the range [0.8, 1.0], the slope of the data is between [0.85, 1.15] and the percentage of the used data must be at least 60%.
- 6) Reflectivity range final selection: Among the accepted iterations, the reflectivity range corresponding to the iteration with a lower RMSE will be selected.

REFERENCES

- ACTRIS, 2022: ACTRIS facilities. Accessed 8 February 2023, <https://www.actris.eu/facilities>.
- Battaglia, A., S. Tanelli, F. Tridon, S. Kneifel, J. Leinonen, and P. Kollias, 2020: Triple-frequency radar retrievals. *Satellite Precipitation Measurement*, V. Levizzani et al., Eds., Advances in Global Change Research, Vol. 67, Springer, 211–229.
- Billault-Roux, A.-C., and Coauthors, 2023: ICE GENESIS: Synergistic aircraft and ground-based remote sensing and in situ measurements of snowfall microphysical properties. *Bull. Amer. Meteor. Soc.*, **104**, E367–E388, <https://doi.org/10.1175/BAMS-D-21-0184.1>.
- Ceccaldi, M., J. Delanoë, R. J. Hogan, N. L. Pounder, A. Protat, and J. Pelon, 2013: From CloudSat-CALIPSO to EarthCARE: Evolution of the DARDAR cloud classification and its comparison to airborne radar-lidar observations. *J. Geophys. Res. Atmos.*, **118**, 7962–7981, <https://doi.org/10.1002/jgrd.50579>.
- Chandrasekar, V., L. Baldini, N. Bharadwaj, and P. L. Smith, 2015: Calibration procedures for Global Precipitation-Measurement ground-validation radars. *URSI Radio Sci. Bull.*, **2015**, 45–73, <https://doi.org/10.23919/URSIRSB.2015.7909473>.
- Cimini, D., and Coauthors, 2020: Towards the profiling of the atmospheric boundary layer at European scale—Introducing the COST Action PROBE. *Bull. Atmos. Sci. Technol.*, **1**, 23–42, <https://doi.org/10.1007/s42865-020-00003-8>.
- Delanoë, J., and R. J. Hogan, 2010: Combined CloudSat-CALIPSO-MODIS retrievals of the properties of ice clouds. *J. Geophys. Res.*, **115**, D00H29, <https://doi.org/10.1029/2009JD012346>.
- , and Coauthors, 2016: BASTA: A 95-GHz FMCW Doppler radar for cloud and fog studies. *J. Atmos. Oceanic Technol.*, **33**, 1023–1038, <https://doi.org/10.1175/JTECH-D-15-0104.1>.
- Dezitter, F., A. Grandin, J.-L. Brenguier, F. Hervy, H. Schlager, P. Villedieu, and G. Zalamansky, 2013: HAIC—High Altitude Ice Crystals. *Fifth AIAA Atmospheric and Space Environments Conf.*, San Diego, CA, Aerospace Research Central, <https://doi.org/10.2514/6.2013-2674>.
- Ewald, F., S. Groß, M. Hagen, L. Hirsch, J. Delanoë, and M. Bauer-Pfundstein, 2019: Calibration of a 35 GHz airborne cloud radar: Lessons learned and intercomparisons with 94 GHz cloud radars. *Atmos. Meas. Tech.*, **12**, 1815–1839, <https://doi.org/10.5194/amt-12-1815-2019>.
- Fox, N. I., and A. J. Illingworth, 1997: The retrieval of stratocumulus cloud properties by ground-based cloud radar. *J. Appl. Meteor.*, **36**, 485–492, [https://doi.org/10.1175/1520-0450\(1997\)036<0485:TROSCP>2.0.CO;2](https://doi.org/10.1175/1520-0450(1997)036<0485:TROSCP>2.0.CO;2).

- Germann, U., 1999: Radome attenuation—A serious limiting factor for quantitative radar measurements? *Meteor. Z.*, **8**, 85–90, <https://doi.org/10.1127/metz/8/1999/85>.
- Grabowski, W. W., H. Morrison, S.-I. Shima, G. C. Abade, P. Dziekan, and H. Pawlowska, 2019: Modeling of cloud microphysics: Can we do better? *Bull. Amer. Meteor. Soc.*, **100**, 655–672, <https://doi.org/10.1175/BAMS-D-18-0005.1>.
- Haggerty, J., and Coauthors, 2019: Detecting clouds associated with jet engine ice crystal icing. *Bull. Amer. Meteor. Soc.*, **100**, 31–40, <https://doi.org/10.1175/BAMS-D-17-0252.1>.
- Hersbach, H., and Coauthors, 2020: The ERA5 global reanalysis. *Quart. J. Roy. Meteor. Soc.*, **146**, 1999–2049, <https://doi.org/10.1002/qj.3803>.
- Hogan, R. J., A. J. Illingworth, and H. Sauvageot, 2000: Measuring crystal size in cirrus using 35- and 94-GHz radars. *J. Atmos. Oceanic Technol.*, **17**, 27–37, [https://doi.org/10.1175/1520-0426\(2000\)017<0027:MCSICU>2.0.CO;2](https://doi.org/10.1175/1520-0426(2000)017<0027:MCSICU>2.0.CO;2).
- , D. Bouniol, D. N. Ladd, E. J. O'Connor, and A. J. Illingworth, 2003: Absolute calibration of 94/95-GHz radars using rain. *J. Atmos. Oceanic Technol.*, **20**, 572–580, [https://doi.org/10.1175/1520-0426\(2003\)20<572:ACOGRU>2.0.CO;2](https://doi.org/10.1175/1520-0426(2003)20<572:ACOGRU>2.0.CO;2).
- Kollias, P., and Coauthors, 2020: The ARM radar network: At the leading edge of cloud and precipitation observations. *Bull. Amer. Meteor. Soc.*, **101**, E588–E607, <https://doi.org/10.1175/BAMS-D-18-0288.1>.
- Küchler, N., S. Kneifel, U. Löhnert, P. Kollias, H. Czekala, and T. Rose, 2017: A W-band radar–radiometer system for accurate and continuous monitoring of clouds and precipitation. *J. Atmos. Oceanic Technol.*, **34**, 2375–2392, <https://doi.org/10.1175/JTECH-D-17-0019.1>.
- Leinonen, J., 2014: High-level interface to T-matrix scattering calculations: Architecture, capabilities and limitations. *Opt. Express*, **22**, 1655–1660, <https://doi.org/10.1364/OE.22.001655>.
- Lemaître, Y., N. Pauwels, and C. Le Gac, 2016: Micro-rain radar en bande X pour la climatologie des propriétés microphysiques des systèmes précipitants: ROXI (Rain Observation with an X-band Instrument). HAL, <https://hal-insu.archives-ouvertes.fr/insu-01407288>.
- Leroy, D., and Coauthors, 2017: Ice crystal sizes in high ice water content clouds. Part II: Statistics of mass diameter percentiles in tropical convection observed during the HAIC/HIWC project. *J. Atmos. Oceanic Technol.*, **34**, 117–136, <https://doi.org/10.1175/JTECH-D-15-0246.1>.
- Liao, L., R. Meneghini, L. Tian, and G. M. Heymsfield, 2009: Measurements and simulations of nadir-viewing radar returns from the melting layer at X and W bands. *J. Appl. Meteor. Climatol.*, **48**, 2215–2226, <https://doi.org/10.1175/2009JAMC2033.1>.
- Liebe, H. J., 1985: An updated model for millimeter wave propagation in moist air. *Radio Sci.*, **20**, 1069–1089, <https://doi.org/10.1029/RS020i005p01069>.
- , 1989: MPM—An atmospheric millimeter-wave propagation model. *Int. J. Infrared Millimeter Waves*, **10**, 631–650, <https://doi.org/10.1007/BF01009565>.
- Mancini, A., J. L. Salazar, R. M. Lebrón, and B. L. Cheong, 2018: A novel instrument for real-time measurement of attenuation of weather radar radome including its outer surface. Part I: The concept. *J. Atmos. Oceanic Technol.*, **35**, 953–973, <https://doi.org/10.1175/JTECH-D-17-0083.1>.
- Matrosov, S. Y., 2009: A method to estimate vertically integrated amounts of cloud ice and liquid and mean rain rate in stratiform precipitation from radar and auxiliary data. *J. Appl. Meteor. Climatol.*, **48**, 1398–1410, <https://doi.org/10.1175/2009JAMC2106.1>.
- Mishchenko, M. I., and L. D. Travis, 1994: T-matrix computations of light scattering by large spheroidal particles. *Opt. Commun.*, **109**, 16–21, [https://doi.org/10.1016/0030-4018\(94\)90731-5](https://doi.org/10.1016/0030-4018(94)90731-5).
- , —, and A. Macke, 1996: Scattering of light by polydisperse, randomly oriented, finite circular cylinders. *Appl. Opt.*, **35**, 4927–4940, <https://doi.org/10.1364/AO.35.004927>.
- Myagkov, A., S. Kneifel, and T. Rose, 2020: Evaluation of the reflectivity calibration of W-band radars based on observations in rain. *Atmos. Meas. Tech.*, **13**, 5799–5825, <https://doi.org/10.5194/amt-13-5799-2020>.
- Nakamura, K., and H. Inomata, 1991: Non-Rayleigh scattering effect in rain observations by an X- and Ka-band dual-wavelength radar. *J. Atmos. Oceanic Technol.*, **8**, 352–362, [https://doi.org/10.1175/1520-0426\(1991\)008<0352:NRSEIR>2.0.CO;2](https://doi.org/10.1175/1520-0426(1991)008<0352:NRSEIR>2.0.CO;2).
- Pappalardo, G., 2017: ACTRIS Aerosol, Clouds and Trace gases Research Infrastructure. *28th Int. Laser Radar Conf.*, Bucharest, Romania, ILRC, 09004, <https://doi.org/10.1051/epjconf/201817609004>.
- Protat, A., J. Delanoë, D. Bouniol, A. J. Heymsfield, A. Bansemmer, and P. Brown, 2007: Evaluation of ice water content retrievals from cloud radar reflectivity and temperature using a large airborne in situ microphysical database. *J. Appl. Meteor. Climatol.*, **46**, 557–572, <https://doi.org/10.1175/JAM2488.1>.
- , and Coauthors, 2009: Assessment of CloudSat reflectivity measurements and ice cloud properties using ground-based and airborne cloud radar observations. *J. Atmos. Oceanic Technol.*, **26**, 1717–1741, <https://doi.org/10.1175/2009JTECHA1246.1>.
- Rosenfeld, D., and W. L. Woodley, 2000: Deep convective clouds with sustained supercooled liquid water down to -37.5°C . *Nature*, **405**, 440–442, <https://doi.org/10.1038/35013030>.
- Scolnik, M. I., 2000: *Radar Handbook*. 3rd ed. Mc Craw-Hill, 1352 pp.
- Tapiador, F. J., J.-L. Sánchez, and E. García-Ortega, 2019: Empirical values and assumptions in the microphysics of numerical models. *Atmos. Res.*, **215**, 214–238, <https://doi.org/10.1016/j.atmosres.2018.09.010>.
- Toledo, F., J. Delanoë, M. Haeffelin, J.-C. Dupont, S. Jorquera, and C. Le Gac, 2020: Absolute calibration method for frequency-modulated continuous wave (FMCW) cloud radars based on corner reflectors. *Atmos. Meas. Tech.*, **13**, 6853–6875, <https://doi.org/10.5194/amt-13-6853-2020>.
- Toledo Bittner, F., 2021: Improvement of cloud radar products for fog surveillance networks: Fog life cycle analyses and calibration methodologies. These doctorat, Institut Polytechnique de Paris, 144 pp., <https://tel.archives-ouvertes.fr/tel-03298445>.
- Tridon, F., A. Battaglia, and S. Kneifel, 2020: Estimating total attenuation using Rayleigh targets at cloud top: Applications in multilayer and mixed-phase clouds observed by ground-based multifrequency radars. *Atmos. Meas. Tech.*, **13**, 5065–5085, <https://doi.org/10.5194/amt-13-5065-2020>.
- , I. Silber, A. Battaglia, S. Kneifel, A. Fridlind, P. Kalogeras, and R. Dhillon, 2022: Highly supercooled riming and unusual triple-frequency radar signatures over McMurdo Station, Antarctica. *Atmos. Chem. Phys.*, **22**, 12467–12491, <https://doi.org/10.5194/acp-22-12467-2022>.
- Trömel, S., A. V. Ryzhkov, B. Hickman, K. Mühlbauer, and C. Simmer, 2019: Polarimetric radar variables in the layers of melting and dendritic growth at X band—Implications for a nowcasting strategy in stratiform rain. *J. Appl. Meteor. Climatol.*, **58**, 2497–2522, <https://doi.org/10.1175/JAMC-D-19-0056.1>.
- Wallace, J. M., and P. V. Hobbs, 2006: *Atmospheric Science: An Introductory Survey*. Vol. 92. Elsevier, 483 pp.

- Wang, Z., and Coauthors, 2012: Single aircraft integration of remote sensing and in situ sampling for the study of cloud microphysics and dynamics. *Bull. Amer. Meteor. Soc.*, **93**, 653–668, <https://doi.org/10.1175/BAMS-D-11-00044.1>.
- Wieland, D. J., M. I. Mishchenko, A. Macke, and B. E. Carlson, 1997: Improved T-matrix computations for large, nonabsorbing and weakly absorbing nonspherical particles and comparison with geometric optics approximation. *Appl. Opt.*, **36**, 4305–4313, <https://doi.org/10.1364/AO.36.004305>.
- Yau, M., and R. R. Rogers, 1996: *A Short Course in Cloud Physics*. Elsevier, 304 pp.
- Yin, J., P. Hoozeboom, C. Unal, H. Russchenberg, F. van der Zwan, and E. Oudejans, 2019: UAV-aided weather radar calibration. *IEEE Trans. Geosci. Remote Sens.*, **57**, 10 362–10 375, <https://doi.org/10.1109/TGRS.2019.2933912>.